CrossMark
click for updates

Hexagonal boron nitride neutron detectors with high detection efficiencies

A. Maity, S. J. Grenadier, J. Li, J. Y. Lin,[a)] and H. X. Jiang[a)]
Department of Electrical and Computer Engineering, Texas Tech University, Lubbock, Texas 79409, USA

Neutron detectors fabricated from ^{10}B enriched hexagonal boron nitride (h-^{10}BN or h-BN) epilayers have demonstrated the highest thermal neutron detection efficiency among solid-state neutron detectors to date at about 53%. In this work, photoconductive-like vertical detectors with a detection area of $1 \times 1\,mm^2$ were fabricated from $50\,\mu m$ thick free-standing h-BN epilayers using Ni/Au and Ti/Al bilayers as ohmic contacts. Leakage currents, mobility-lifetime ($\mu\tau$) products under UV photoexcitation, and neutron detection efficiencies have been measured for a total of 16 different device configurations. The results have unambiguously identified that detectors incorporating the Ni/Au bilayer on both surfaces as ohmic contacts and using the negatively biased top surface for neutron irradiation are the most desired device configurations. It was noted that high growth temperatures of h-^{10}BN epilayers on sapphire substrates tend to yield a higher concentration of oxygen impurities near the bottom surface, leading to a better device performance by the chosen top surface for irradiation than by the bottom. Preferential scattering of oxygen donors tends to reduce the mobility of holes more than that of electrons, making the biasing scheme with the ability of rapidly extracting holes at the irradiated surface while leaving the electrons to travel a large average distance inside the detector at a preferred choice. When measured against a calibrated ^{6}LiF filled micro-structured semiconductor neutron detector, it was shown that the optimized configuration has pushed the detection efficiency of h-BN neutron detectors to 58%. These detailed studies also provided a better understanding of growth-mediated impurities in h-BN epilayers and their effects on the charge collection and neutron detection efficiencies. *Published by AIP Publishing.*
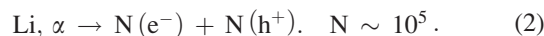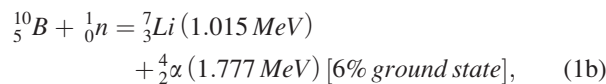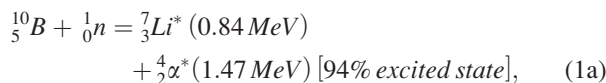https://doi.org/10.1063/1.5017979

I. INTRODUCTION

Hexagonal boron nitride (h-BN), a wide bandgap ($\sim 6.5\,eV$) semiconductor, known for its deep ultraviolet photonic applications,[1–7] has emerged as an outstanding neutron detector material[8–14] due to the fact that the B-10 (^{10}B) isotope has a large capture cross section for thermal neutrons (3840 b or $3.84 \times 10^{-21}\,cm^2$). Special nuclear materials (SNMs) tend to emit neutrons through fission reactions. Thus, neutron detectors with improved detection efficiencies and sensitivities are highly sought after since neutrons are an exceedingly specific indicator of fissile materials. Neutron detectors are also an indispensable tool in geothermal and well-logging for the determination of the formation properties, including the porosity and water (and/or H_2) content.[15] Pressurized $^3_2 He$ (He-3) gas tube detectors have been the dominant deployed technology for various applications due to the high thermal neutron capture cross-section of $^3_2 He$ (~ 5330 b) and their high technology maturity. However, being a gas, $^3_2 He$ contains very low atomic density corresponding to a long absorption length for thermal neutrons, making $^3_2 He$ detectors inherently bulky. Other shortcomings of $^3_2 He$ detectors are the need of high pressurization (e.g., 20 atm for 2.25-in. diameter tubes), high voltage operation ($>1000\,V$), and slow response speed ($\sim ms$). These attributes prohibit flexibilities in detector design, form factors, and increase manufacturing and maintenance costs. Therefore, solid-state neutron detectors that have the performance of $^3_2 He$ detectors without their drawbacks are highly sought-after technologies.[8–14,16–22]

As a semiconductor, the density of atoms that can interact with thermal neutrons in 100% ^{10}B-enriched h-BN [N(^{10}B) $= 5.5 \times 10^{22}/cm^3$] is about 550 times higher than that in He-3 gas pressurized at 4 atm, providing an absorption length (λ) of thermal neutrons in h-^{10}BN of only $47\,\mu m$, where $\lambda = (3.84 \times 10^{-21}\,cm^2 \times 5.5 \times 10^{22}/cm^3)^{-1} = 0.0047\,cm$.[13,14] This length scale is negligibly small compared to the diameters of typical $^3_2 He$ detectors. The absorption of a thermal neutron by a ^{10}B atom induces the following nuclear reaction inside h-^{10}BN:[23]

$$\begin{aligned} ^{10}_5 B + {}^1_0 n = {}^7_3 Li^* \,(0.84\,MeV) \\ + {}^4_2 \alpha^* (1.47\,MeV)\,[94\%\ excited\ state], \end{aligned} \quad (1a)$$

$$\begin{aligned} ^{10}_5 B + {}^1_0 n = {}^7_3 Li \,(1.015\,MeV) \\ + {}^4_2 \alpha \,(1.777\,MeV)\,[6\%\ ground\ state], \end{aligned} \quad (1b)$$

$$Li, \alpha \rightarrow N\,(e^-) + N\,(h^+). \quad N \sim 10^5. \quad (2)$$

The detection of neutrons is accomplished in two sequential processes. The first is the neutron absorption process described by Eq. (1) in which the nuclear reaction creates Li and α daughter particles with large kinetic energies. Equation (2) describes the subsequent process of charge carrier generation by Li and α particles and the collection of radiation-generated electrons (e^-) and holes (h^+). In BN

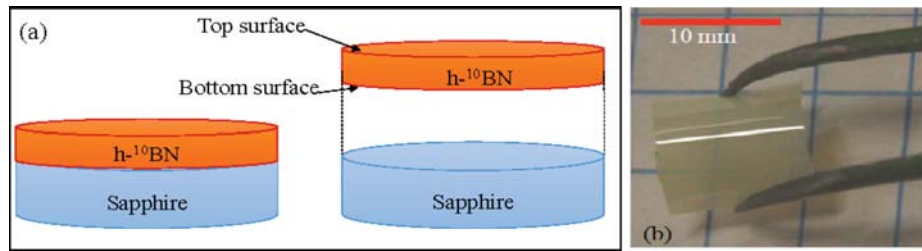a)Electronic addresses: jingyu.lin@ttu.edu and hx.jiang@ttu.edu

FIG. 1. (a) Schematic representation of h-^{10}BN epilayers grown on sapphire and obtaining freestanding h-^{10}BN epilayers via mechanical separation. Top and bottom surfaces are indicated with respect to the original interface between h-^{10}BN and sapphire. (b) Optical image of a freestanding h-^{10}BN epilayer.

detectors, these two sequential processes occur in the same BN layer, making high detection efficiency possible.

Recently, we have successfully produced freestanding, flexible, and single crystal h-^{10}BN epilayer wafers of 4 in. diameter with a thickness of about 50 μm.[13,14] Photoconductive-like detectors with a detection area up to 9 mm^2 fabricated from these materials possess a rather high thermal neutron detection efficiency among solid-state neutron detectors at about 53% when measured against a calibrated ^{6}LiF filled micro-structured semiconductor neutron detector.[13,14] These recent progresses have opened up new opportunities to obtain practical h-BN detectors that potentially offer the advantages of increased detection efficiency and operating temperature and ruggedness, reduced size and weight, no pressurization, lower operating voltage and power consumption, larger/faster signals in extreme environments, and lower costs for fabrication, operation, and maintenance compared with ^3_2He detectors.

Based on the well-developed and understood ohmic contact formation on p-type GaN[24] and previous hints of unintentionally doped h-BN that tends to exhibit p-type conduction,[25] so far, we have adopted Ni (15 nm)/Au (20 nm) bilayers as the ohmic contacts for h-BN for quick assessments of electrical properties and for device demonstration.[13,14] However, due to the high resistive nature, it is challenging to determine the actual conductivity type of unintentionally doped h-BN. As such, it is still worthwhile to investigate the well-known n-type ohmic contacts for III-nitrides, such as Ti/Al bilayer. Furthermore, considering the fact that sapphire was used as a substrate and that the growth of thick layers of h-BN requires several hours to complete at high temperatures, the bottom surface of h-BN after liftoff from sapphire is not necessarily identical to the top surface in terms of impurity contents. Consequently, there rise ambiguities regarding the optimal excitation and biasing configurations with respect to the h-BN surfaces to enable the same detector to achieve the best performance. In this work, we

aimed to identify the optimal radiation direction and the biasing polarity, as well as the most favored choice of ohmic contact materials for obtaining a further enhanced detection efficiency for neutron detectors fabricated from the same batch of h-BN materials.

II. EXPERIMENTS

As schematically illustrated in Fig. 1(a), h-^{10}BN epilayers of a thickness of about 50 μm were grown using metal organic chemical vapor deposition (MOCVD) on c-plane sapphire (Al$_2$O$_3$) substrates of 4-in. diameter. Trimethylboron (TMB) with a vendor-specified ^{10}B isotope enrichment of 99.9% and ammonia (NH$_3$) were used as the precursors for the growth of h-^{10}BN epilayers. The epi-growth temperature was >1400 °C in order to obtain h-BN epilayers with high crystalline quality. Due to the unique layered structure of h-BN and the difference in thermal expansion coefficients between h-BN and the sapphire substrate, h-BN epilayers with a sufficient thickness automatically separate from substrates during cooling down after growth, allowing the realization of freestanding h-BN wafers. However, these freestanding epilayers differ from true bulk materials in several aspects. First, these materials are flexible [Fig. 1(b)]. The second aspect is that the high growth temperatures together with the use of the sapphire substrate could introduce more defects associated with oxygen impurities near the bottom surface compared to the top surface. Moreover, the density of radiation-generated charge carriers is the highest near the irradiated surface and exponentially decreases with the thickness of the material as follows: $n(x) \sim I_0 e^{-x/\lambda}$, where I$_0$ denotes the initial radiation intensity and λ is the absorption length (and more specifically, $\lambda \sim 47 \mu$m for thermal neutrons in h-^{10}BN). These scenarios are illustrated in Fig. 2, which clearly shows that the choice of the irradiation surface could matter due to the asymmetric
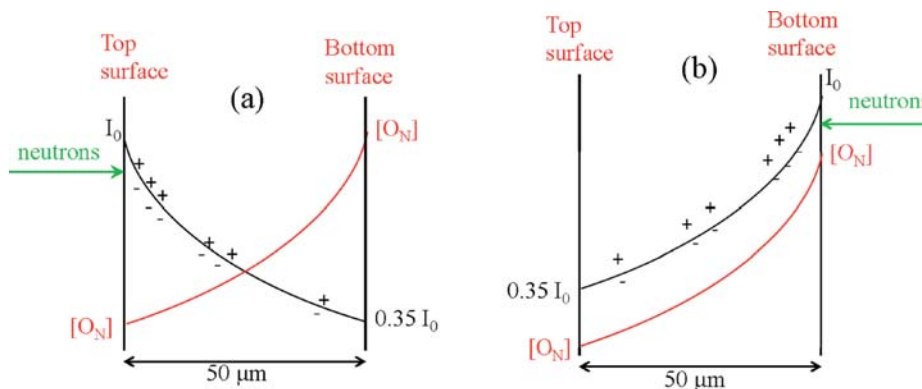

FIG. 2. Schematic illustrations of the O$_N$ defect (oxygen impurities occupying nitrogen sites) distribution and radiation-generated charge carriers inside h-^{10}BN detectors for radiation entered from the (a) top surface and (b) bottom surface.
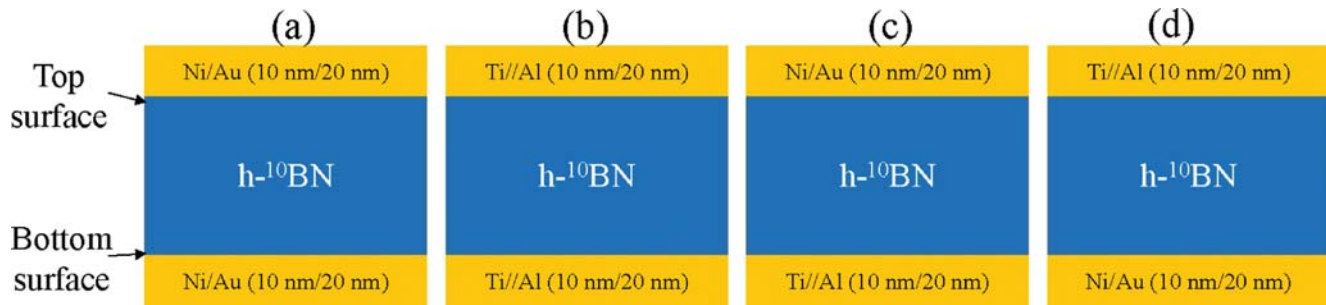
FIG. 3. Schematic illustrations of the photoconductive-type of neutron detectors fabricated from freestanding h-^{10}BN epilayers used in this work: (a) Detectors with the Ni/Au bilayer deposited on both top and bottom surfaces. (b) Detectors with the Ti/Al bilayer deposited on both top and bottom surfaces. (c) Detectors with the Ni/Au bilayer deposited on the top surface and the Ti/Al bilayer deposited on the bottom surface. (d) Detectors with the Ti/Al bilayer deposited on the top surface and the Ni/Au bilayer deposited on the bottom surface.

distribution of oxygen defects near the two sample surfaces, as the secondary-ion mass spectrometry measurements revealed that the oxygen impurity concentration is about 3 times higher near the bottom surface than that near the top. Finally, a positively (negatively) biased irradiated surface extracts electrons (holes) more quickly upon radiation absorption, whereas holes (electrons) have to travel a larger average distance inside h-BN before being collected by the opposite electrode. The presence of a specific type of defect could affect the carrier transport properties differently depending upon the carrier type. Therefore, bias configurations could also affect the overall charge collection efficiency.

With the above discussed ambiguities being considered, we have fabricated h-BN detectors which incorporate 4 different contact configurations, as schematically shown in Fig. 3. Ni/Au (10 nm/20 nm) and Ti/Al (10 nm/20 nm) bilayers were deposited on freestanding h-^{10}BN using e-beam evaporation. Shadow masks were used to fabricate 1 mm × 1 mm devices with a metal bilayer deposited on each surface in all 4 possible combinations. No postdeposition thermal annealing process was implemented. For each of the device configurations, there are two possible biasing conditions, either positively biasing the top surface or positively biasing the bottom surface and therefore giving 8 possible configurations. Moreover, as shown in Fig. 2, for each device with a given bias configuration, we could have two possibilities of irradiation directions, irradiating the detector either through the top or through the bottom surface. Therefore, we ended up probing the transport properties and the detection efficiencies of a total of 16 different device configurations.

III. EXPERIMENTAL RESULTS AND DISCUSSION

As shown in Eqs. (1) and (2), the detection of neutrons by h-BN relies on the charge carrier collection. The process is assisted by the application of an external bias voltage that generates a short current pulse that is further integrated, amplified, and shaped in the detector electronics and eventually digitized to produce a pulse height spectrum. The presence of a high noise level increases the setting point of low level discriminator and consequently decreases the signal to noise ratio, which could exclude a fraction of the actual counts from being detected. It is well established that the

"shot noise" in the detector electronics is directly proportional to the detector's leakage (or dark) current, I_d.[26] Therefore, the leakage current is one of the most important parameters in determining the sensitivity of a neutron detector. Dark I–V characteristics were measured for each of the four device configurations shown in Fig. 3, all of which exhibit nearly linear I–V characteristics. Figure 4 shows the dark I–V characteristics of two representative device configurations, and the results demonstrate that the choice of these metals provides an adequate ohmic behavior. However, the detector shown in Fig. 3(a) (with the Ni/Au bilayer on both surfaces) exhibits the lowest leakage currents (I_d) at all bias voltages among the four types of fabricated devices, and more specifically, its I_d value at 400 V is about 35 times
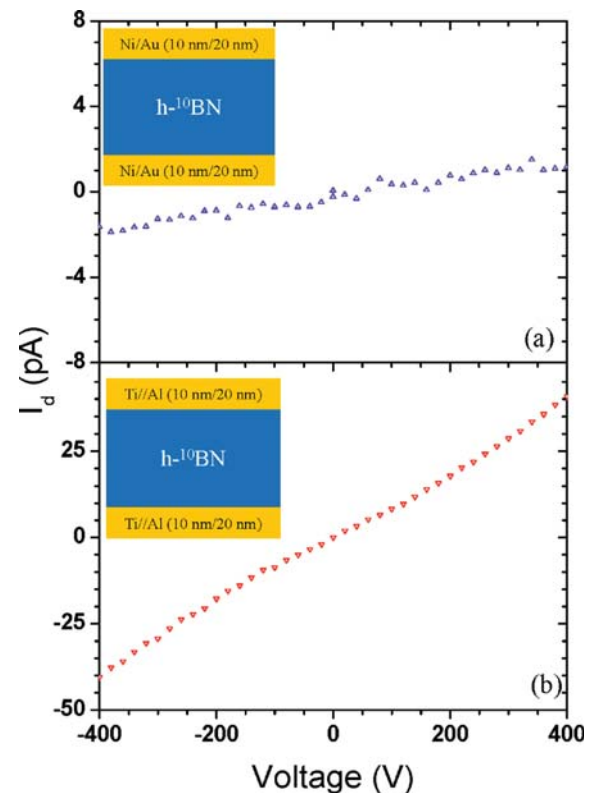

FIG. 4. Dark I-V characteristics measured for the device configuration shown in (a) Fig. 3(a) and (b) Fig. 3(b).

lower than that of the detector shown in Fig. 3(b) (with the Ti/Al bilayer on both surfaces). The measured electrical resistivity (ρ) of the detector with the Ni/Au bilayer on both surfaces is about $7.1 \times 10^{14}\,\Omega$ cm, whereas ρ for the detector with the Ti/Al contact on both surfaces is about $0.2 \times 10^{14}\,\Omega$ cm. It is this large resistivity of h-^{10}BN that contributes to very low leakage currents for h-^{10}BN detectors, which in turn translates to low noise associated with the detection electronics system.[14] Hence, the results shown in Fig. 4 suggest that detectors with a configuration shown in Fig. 3(a) (with the Ni/Au bilayer on both surfaces) are more favorable for neutron detector applications. Another advantage of h-BN is its relatively small in-plane dielectric constant $\varepsilon \sim 4$,[27] which further helps to keep the capacitance and hence the noise level low for h-BN detectors.

The product of mobility and lifetime ($\mu\tau$) is another key parameter that determines the overall performance of detectors. This product is a combination of the carrier mobility (μ) within the material and the mean lifetime (τ) of the radiation-generated carriers that travel freely before they are trapped. Most of the radiation-generated charge carriers inside a detector can be collected by the electrodes when the condition of recombination lifetime (τ) $\geq$ transit time (τ_t) is satisfied, i.e., $\mu\tau \geq L^2/V$ ($\tau_t = L/\mu E$, $E = V/L$), or equivalently $\frac{L^2}{V\mu\tau} \leq 1$, where V is the applied voltage and L is the transit length (the distance between the two electrodes or the h-BN layer thickness in the present case). The $\mu\tau$ product determines the conduction capability of radiation-generated carriers and hence the charge collection efficiency. For a given device dimension, enhancing the $\mu\tau$ product would increase the detection efficiency. This parameter is influenced by crystalline quality and the density of impurities/defects introduced during the crystal growth and device fabrication processes.

In contrast to thermal neutron absorption in h-BN with an absorption length of $\lambda \sim 47\,\mu$m, the optical absorption length of the above bandgap photons in h-BN is only about 14.5 nm.[4,28] Thus, most of the above bandgap photons are absorbed within about 70 nm (5λ) from the irradiated surface. Depending upon the polarity of the illuminated surface, specific charge carriers (hole or electron) can be selected for transport in the direction perpendicular to the sample surface (in the direction of the c-axis). The negatively (positively) biased illuminated surface immediately extracts holes (electrons) upon photo-generation, therefore allowing only electrons (holes) to transport to the opposite electrode to be collected at a later time (τ_t). This property enables us to characterize the electrical transport properties of holes and electrons separately. For instance, when a 50 μm thick h-^{10}BN detector is biased in the configuration shown in the inset of Fig. 5(a), holes are swiped away at the negatively biased irradiated top surface and only electrons travel inside the material, and therefore, this configuration allows us to obtain the $\mu\tau$ value for electrons.

The $\mu\tau$ products of charge carriers were measured for each of the 16 configurations under UV excitation using a deuterium UV lamp (DS421, Acton Research Corporation). Fitting the photocurrents measured for all 16 different configurations with Many's equation[29] allows us to obtain the $\mu\tau$-products

$$I_i(V) = I_{0,i}\left[\frac{V\mu_i\tau_i\left(1 - e^{-\frac{L^2}{V\mu_i\tau_i}}\right)}{L^2\left(1 + \frac{s_iL}{\mu_iV}\right)}\right].\,(i = e, h). \quad (3)$$

Here, the saturation current is denoted as I_0, and $\mu_e\tau_e$ ($\mu_h\tau_h$) and s_e (s_h) are the mobility-lifetime product and surface
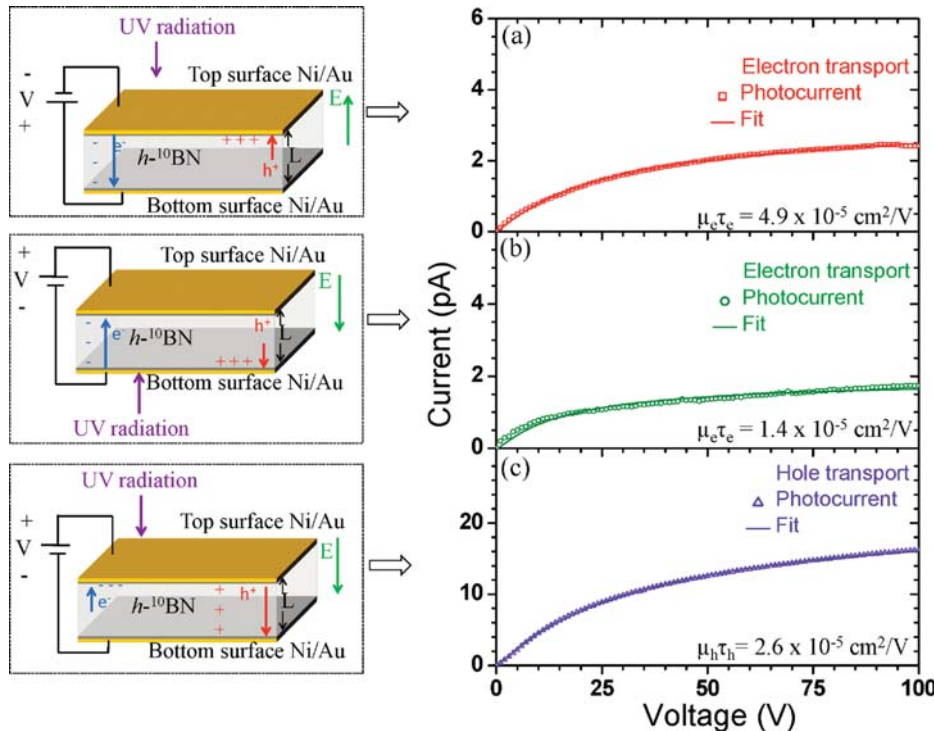

FIG. 5. Photocurrent-voltage characteristics measured under UV radiation for three different device configurations.

recombination velocity for electrons (holes), respectively. I–V curves under UV light excitation for three representative configurations are also shown in Fig. 5 and were fitted with Eq. (3) to extract $\mu\tau$ values.

Arguments were implemented based on the $\mu\tau$-products while aiming at identifying the optimum detector configuration. Devices with the same type of metal bilayers on the both sides were chosen to compare the effects of different irradiation directions. Symmetric metal contacts are important in this comparison so that any effects resulting from contacts on the $\mu\tau$-products could be avoided. The results shown in Figs. 5(a) and 5(b) for the device with the Ni/Au bilayer on both surfaces clearly show that using the top surface for irradiation yields a higher $\mu\tau$-product value than using the bottom surface for irradiation (4.9×10^{-5} cm^2/V vs 1.4 $\times 10^{-5}$ cm^2/V). A similar conclusion was obtained for the device with the Ti/Al bilayer on both the surfaces. The results corroborate the speculation that the defect density near the bottom surface is higher than that near the top surface. While keeping the radiation direction and biasing condition fixed, comparisons of $\mu\tau$-products between different metal configurations yield the device configuration as shown in Fig. 3(a) (with the Ni/Au bilayer on both surfaces), being the preferred contact scheme, consistent with the leakage current (I_d) measurement results shown in Fig. 4. Furthermore, comparison between biasing scenarios for the same device with the ideal irradiation direction (using the top surface for irradiation) shown in Figs. 5(a) and 5(c) indicates that the specific voltage biasing scheme with the ability of rapidly extracting holes at the irradiated surface while leaving the electrons to travel a large average distance to the opposite electrode is a preferred choice, i.e., the device configuration shown in Fig. 5(a) is more favored over that of Fig. 5(c). We noted that the measured $\mu\tau$ products for electrons in Fig. 5(b) and for holes in Fig. 5(c) are about the same as the previous reported values.[14] In our previous work, however, the effects of biasing polarity were not noted, whereas the radiation direction was set to enter from the bottom surface.[14]

We also noted that the measured $\mu\tau$ products for all 16 device configurations are greater than 10^{-6} cm^2/V with a lowest value of $\mu_h\tau_h = 1.8 \times 10^{-6}$ cm^2/V for the device configuration shown in Fig. 3(b) with hole transport. Figure 6 plots $\frac{L^2}{V\mu\tau}$ vs. V for various $\mu\tau$-product values, which reveals that the charge collection condition of $\frac{L^2}{V\mu\tau} \leq 1$ is satisfied for all 16 device configurations at V > 100 V. The value of $\frac{L^2}{V\mu\tau}$ at 200 V is smaller than 1% when the $\mu\tau$-product is greater than 10^{-5} cm^2/V. Thermal neutron detection efficiencies for all 16 possible device configurations were measured at 200 V to ensure that most radiation-generated charge carriers can be collected by the electrodes, and the results further corroborate the conclusion drawn from both the $\mu\tau$-product and leakage current (I_d) measurements as discussed below.

To characterize the thermal neutron responses of all 16 device configurations, we have constructed a neutron source system, as schematically shown in Fig. 7(a).[9–11] The system design was adopted from the thesis work of Clinton[17,30] and
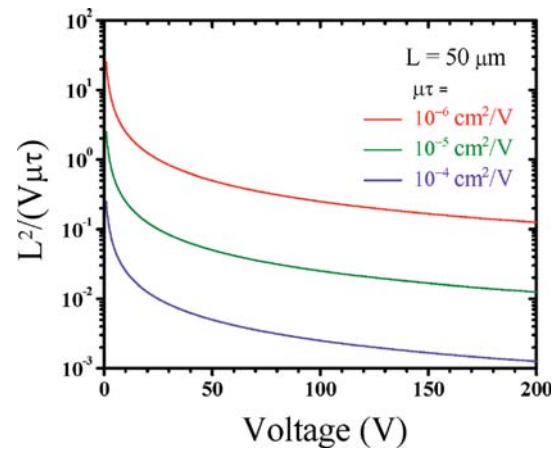
FIG. 6. Plot of L^2/(V$\mu\tau$) vs. bias voltage (V) for $\mu\tau = 10^{-6}$, 10^{-5}, and 10^{-4} cm^2/V for 50 μm thick h-^{10}BN detectors.

based on a depleted sealed source, model 100 californium-252 source (^{252}Cf) which contained 4.2 μg of active ^{252}Cf from Frontier Technology, emitting fission neutrons, moderated by a high density polyethylene (HDPE) block. The experimental geometry and HDPE size and thickness are identical to those described in the thesis.[30] The ^{252}Cf source has a half-life of 2.645 years. At the time of this measurement, the source has a radioactivity of 0.70 mCi, providing a neutron flux of $\sim 3.01 \times 10^6$ neutrons/s with an average energy of 0.7 MeV. If the neutron source is placed at position
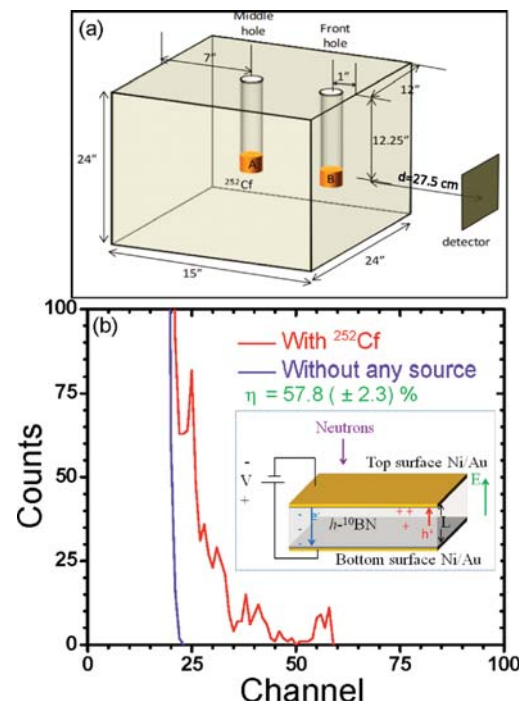
FIG. 7. (a) Schematic diagram of the thermal neutron source consisting of a ^{252}Cf source in conjunction with a moderator constructed from a high density polyethylene (HDPE) block. (b) Nuclear reaction pulse height spectrum of a ^{10}h-BN detector with the device configuration shown in Fig. 5(a) (also shown in the inset) under thermal neutron radiation. The neutron response was measured by placing the detector at 30 cm away from the ^{252}Cf source moderated by a one-inch thick high density polyethylene (HDPE) moderator at a bias voltage of 200 V for 15 min.

"A" shown in Fig. 7(a), most fast neutrons are stopped by the HDPE moderator. If the neutron source is placed at position "B," most neutrons emerging from the front surface of the HDPE moderator are thermal neutrons. Moreover, based on the Monte Carlo N particle code simulations, which modeled the interactions of neutrons with hydrogen atoms in the HDPE moderator, the conversion ratio for the neutron flux from the ^{252}Cf source to thermal neutrons at a point in the air that is 10 cm away from the moderator's surface is 2.43×10^{-4}.[30] Raw thermal neutron count rates were taken from an unmoderated ^{3}He rate meter at varying d, where d is the distance from the front surface of the moderator housing, and the results revealed that the thermal neutron counts are inversely proportional to d^2.[9] This means that the point source model can be appropriately applied to calculate the thermal neutron flux (Φ) ratio at different distances according to $\frac{\Phi_2}{\Phi_1} = \frac{d_1^2}{d_2^2}$.

Each detector was placed inside a light-tight box and at 30 cm away from the source, i.e., 27.5 cm from the front surface of the HDPE. Charge carriers generated inside the h-^{10}BN detector due to deceleration of high energy daughter particles (^7_3Li, $^4_2\alpha$), which are the byproducts of the nuclear reaction between ^{10}B and thermal neutron, were collected by electrodes with the aid of an external bias voltage (200 V), and a short current pulse was subsequently created. This current pulse of neutron response was integrated into a voltage pulse through a charge sensitive preamplifier (Cremat Inc. model CR-110) with a gain of 1.4 V/pC, which was further amplified and shaped using a Gaussian shaping amplifier CR200 (Cremat Inc.) with a full-width at half maximum (FWHM) of 4.7 μs. This Gaussian shaped pulse was then digitized using a multichannel analyzer (MCA) from Amptek (model 8000D) to produce a pulse height spectrum. The dark response was recorded for each detector configuration in the absence of the ^{252}Cf source. The neutron incident rate on the detector ($\sim$1 n/s) was much slower than the system response, and hence, one pulse corresponded to the detection of a single neutron. To obtain the total neutron counts, a neutron spectrum was integrated beyond the highest channel of the dark spectrum. The pulse height spectrum for the most preferred device configuration identified through I_d and $\mu\tau$ measurements is depicted in Fig. 7(b). A certified ^{6}LiF filled Si microstructured neutron detector (MSND Domino^{TM} V4)[18,31] with a detection area of 4 cm^2 obtained from Radiation Detection Technology, Inc., with a specified thermal neutron detection efficiency of $\eta_{MSND} = 30\ (\pm 1)\%$ was used to calibrate the thermal neutron detection efficiency of h-^{10}BN detectors. Our h-^{10}BN detector with a device configuration shown in the inset of Fig. 7(b) [or Fig. 5(a)] produced a count rate of 0.6 ($\pm$0.01) n/s which corresponds to a count rate per unit area of $C_{10BN} = 59.9\ (\pm 1.3)$ n/s cm^2. A count rate per unit area of $C_{MSND} = 31.1\ (\pm 0.1)$ n/s cm^2 was obtained from MSND by placing it at the same position as the h-^{10}BN detectors. Hence, the thermal neutron detection efficiency can be obtained as

$$\eta_{^{10}BN} = \frac{C_{^{10}BN}}{C_{MSND}} \times \eta_{MSND} = \frac{59.9\ (\pm 1.3)}{31.1\ (\pm 0.1)} \times 30\ (\pm 1.0)\%$$
$$= 57.8\ (\pm 2.3)\%. \tag{4}$$

Among all the configurations tested, devices incorporating Ni/Au on both surfaces delivered detection efficiencies $\geq$53% for different biasing and irradiation configurations, whereas devices incorporating Ti/Al on both surfaces delivered detection efficiencies $\leq$45% for different biasing and irradiation configurations. The most preferred device configuration shown in the inset of Fig. 7(b) [or Fig. 5(a)] which incorporates the Ni/Au bilayer on both surfaces with the top irradiated surface negatively biased delivered the highest detection efficiency of $\eta \approx$ 58%. It is important to point out that the BN interaction with gamma photons is exceptionally low due to the fact that BN is composed of low atomic number elements.[9,11] Our previous measurement results have demonstrated that h-BN detectors have a negligible response to γ-photons produced by ^{137}Cs decay with an energy at 0.662 MeV and possess a neutron-gamma rejection ratio larger than 10^6.[9,11]

Corroborating with the leakage current and $\mu\tau$-product results, the measured neutron detection efficiency results also indicate that one of the prominent effects on the detector performance is the choice of ohmic contact material and that the Ni/Au bilayer is the preferred choice over the Ti/Al bilayer. The second effect is the biasing polarity, and the results point to the fact that a biasing scheme that allows electrons to travel a larger average distance than holes is preferred in these h-BN epilayers. This could be related to the fact that electrons have a higher drift mobility than holes in this batch of h-BN epilayers grown under high temperatures, in which oxygen-related defects preferentially scatter/trap holes over electrons. Finally, the device performs better when radiation is entered from the top surface. We attribute this to the presence of a higher concentration of oxygen-related defects near the bottom surface than the top surface due to the high growth temperature and long growth time which likely caused oxygen atoms to diffuse from the sapphire substrate to h-^{10}BN. When the charge carriers are initially generated in the region with a lower defect concentration (near the top surface), a scenario illustrated in Fig. 2(a), they are able to quickly attain high velocities under an external applied electric field. The high velocity lowers the probability of carriers being trapped by the defects near the bottom surface. On the other hand, when the charge carriers are initially generated in the high defect content region (near the bottom surface), a situation shown in Fig. 2(b), more carriers are trapped before they even have the chance to accelerate toward the top electrode.

To determine the energy level of the dominant impurities, we have measured I–V characteristics of the device with the Ni/Au bilayer on both surfaces [Fig. 3(a)] at different temperatures, and the results are shown in Fig. 8(a), from which we extracted the sample resistances (R) at different temperatures. As expected, the dark resistance decreases with increasing temperature. Assuming that the change in mobility (μ) with temperature is negligibly small within the measurement temperature range, R of the film is
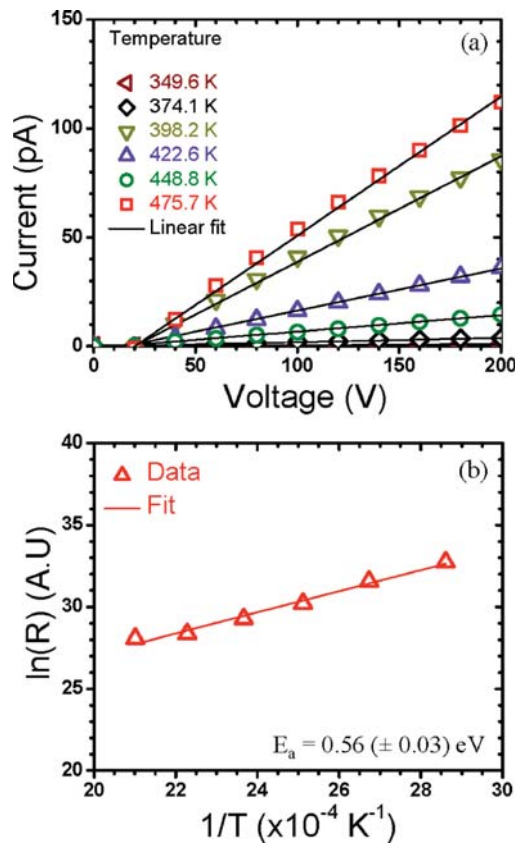
$$R \propto e^{\frac{E_a}{K_B T}}. \tag{5}$$

FIG. 8. (a) Dark I-V characteristics measured for the device configuration shown in Fig. 3(a) at different temperatures, from which the temperature dependence of the sample resistance (R) can be extracted. (b) An Arrhenius plot of R, ln (R) vs 1/T, and the solid line is a linear fit.

Here, E_a is the energy level of the involved defect and K_B is the Boltzmann constant. A linear fitting of the Arrhenius plot of ln(R) v 1/T provides a value of $E_a = 0.56$ (± 0.03) eV. It is this energy level that controls the dark currents of this batch of h-BN devices. Our previous works have indicated that the dominant native and point defects in h-BN epilayers are (a) nitrogen vacancy (V_N) which acts as a shallow donor with an energy level of about 0.1 eV below the conduction band and (b) V_N related defects such as carbon occupying nitrogen site (C_N) which behaves like a deep acceptor with an energy level of about 2.3 eV above the valence band.[32] Apart from these native and point defects, high growth temperature mediated oxygen diffusion from the sapphire substrate is likely to create O_N (oxygen occupying nitrogen site) which behaves like a donor. The measured value of $E_a \sim 0.56$ eV from the temperature-dependent dark I–V characteristics can most probably be attributed to the presence of the oxygen donor. Being a donor, its presence leads to selective scattering/trapping of holes over electrons, which reduces the mobility of holes more than electrons. In other words, the presence of oxygen donor impurities makes electrons (holes) being the majority (minority) carriers in this batch of h-BN materials. This explains why the device performs better when its configuration supports electron transport inside h-BN.

In summary, considering all the results based on the leakage current, photo-excited $\mu\tau$-product, and neutron detection efficiency measurements, we have identified the desired detector configuration for providing the optimum performance. The Ni/Au bilayer has proved to be the better ohmic contact for h-^{10}BN neutron detectors over Ti/Al. High temperature and longtime growth of h-^{10}BN epilayers on the sapphire substrate incorporated more oxygen donor impurities near the bottom surface than the top, leading to a better charge carrier collection by chosen the top surface for irradiation than the bottom. Scattering from oxygen donors reduced the mobility of holes more than electrons, making the device scheme allow electron transport inside the material to be preferred over hole transport. Our results provide useful insights into the effects of metal contacts, radiation directions, and bias voltage polarities on the electrical transport properties and detection efficiencies of neutron detectors based on vertical freestanding h-^{10}BN epilayers. By adopting Ni/Au bilayers on both surfaces as ohmic contacts and using the negatively biased top surface for neutron irradiation, we have gained an improvement in the detection efficiency and pushed the detection efficiency of h-BN detectors to 58% over the previous value of 53%, as calibrated against a certified ^{6}LiF filled Si microstructured neutron detector (MSND Domino V4 from Radiation Detection Technology, Inc.). This is significant considering that it is highly challenging and time-consuming to gain improvements in the overall material quality of h-BN epilayers through optimization of MOCVD growth processes. The present results also indicate that finding ways to minimize oxygen impurity diffusion from the sapphire substrate during h-BN epilayers growth while maintaining high crystalline quality will be beneficial to the detector performance.

[1]K. Watanabe, T. Taniguchi, and H. Kanda, Nat. Mater. **3**, 404 (2004).

[2]Y. Kubota, K. Watanabe, O. Tsuda, and T. Taniguchi, Science **317**, 932 (2007).

[3]K. Watanabe, T. Taniguchi, T. Niiyama, K. Miya, and M. Taniguchi, Nat. Photonics **3**, 591 (2009).

[4]J. Li, S. Majety, R. Dahal, W. P. Zhao, J. Y. Lin, and H. X. Jiang, Appl. Phys. Lett. **101**, 171112 (2012).

[5]S. Majety, J. Li, X. K. Cao, R. Dahal, B. N. Pantha, J. Y. Lin, and H. X. Jiang, Appl. Phys. Lett. **100**, 061121 (2012).

[6]X. K. Cao, B. Clubine, J. H. Edgar, J. Y. Lin, and H. X. Jiang, Appl. Phys. Lett. **103**, 191106 (2013).

[7]R. Dahal, J. Li, S. Majety, B. N. Pantha, X. K. Cao, J. Y. Lin, and H. X. Jiang, Appl. Phys. Lett. **98**, 211110 (2011).

[8]J. Li, R. Dahal, S. Majety, J. Y. Lin, and H. X. Jiang, Nucl. Instrum. Methods Phys. Res., Sect. A **654**, 417 (2011).

[9]T. C. Doan, S. Majety, S. Grenadier, J. Li, J. Y. Lin, and H. X. Jiang, Nucl. Instrum. Methods Phys. Res., Sect. A **748**, 84 (2014).

[10]T. C. Doan, S. Majety, S. Grenadier, J. Li, J. Y. Lin, and H. X. Jiang, Nucl. Instrum. Methods Phys. Res., Sect. A **783**, 121 (2015).

[11]T. C. Doan, J. Li, J. Y. Lin, and H. X. Jiang, AIP Adv. **6**, 075213 (2016).

[12]K. Ahmed, R. Dahal, A. Weltz, J. J.-Q. Lu, Y. Danon, and I. B. Bhat, Appl. Phys. Lett. **110**, 023503 (2017).

[13]A. Maity, T. C. Doan, J. Li, J. Y. Lin, and H. X. Jiang, Appl. Phys. Lett. **109**, 072101 (2016).

[14]A. Maity, S. J. Grenadier, J. Li, J. Y. Lin, and H. X. Jiang, Appl. Phys. Lett. **111**, 033507 (2017).

[15]J. Neal, L. Boatner, Z. Bell, H. Akkurt, and M. McCarthy, "Evaluation of neutron and gamma detectors for high-temperature well-logging applications," in *Future of Instrumentation International Workshop (FIIW)* (2011), pp. 172–175.

[16]Q. Shao, L. F. Voss, A. M. Conway, R. J. Nikolic, M. A. Dar, and C. L. Cheung, Appl. Phys. Lett. **102**, 063505 (2013).

[17]R. Dahal, K. C. Huang, J. Clinton, N. LiCausi, J. Q. Lu, Y. Danon, and I. Bhat, Appl. Phys. Lett. **100**, 243507 (2012).

[18]S. L. Bellinger, R. G. Fronk, W. J. McNeil, T. J. Sobering, and D. S. McGregor, IEEE Trans. Nucl. Sci. **59**, 167 (2012).

[19]A. M. Conway, R. J. Nikolic, and T. F. Wang, in *Proceedings of the International Semiconductor Device Research Conference* (IEEE, New York, 2007), p. 589.

[20]K. Osberg, N. Schemm, S. Balkir, J. O. Brand, M. S. Hallbeck, P. A. Dowben, and M. W. Hoffman, IEEE Sens. J. **6**, 1531 (2006).

[21]D. S. McGregor, T. C. Unruh, and W. J. McNeil, Nucl. Instrum. Methods Phys. Res., Sect. A **591**, 530 (2008).

[22]Y. B. Losovyj, I. Ketsman, A. Sokolov, K. D. Belashchenko, P. Dowben, J. Tang, and Z. Wang, Appl. Phys. Lett. **91**, 132908 (2007).

[23]G. F. Knoll, *Radiation Detection and Measurement*, 4th ed. (John Wiley & Sons, 2010).

[24]S. Nakamura, S. J. Pearton, and G. Fasol, *The Blue Laser Diode - The Complete Story* (Springer-Verlag, Berlin, Heidelberg, 1997/2000).

[25]M. Lu, A. Bousetta, A. Bensaoula, K. Waters, and J. A. Schultz, Appl. Phys. Lett. **68**, 622 (1996).

[26]H. G. Spieler and E. E. Haller, IEEE Trans. Nucl. Sci. **32**, 419 (1985).

[27]A. J. Gatesman, R. H. Giles, and J. Waldman, in *1991 MRS Fall Meeting, Symposium G-Wide Band-Gap Semiconductors* (Mater. Res. Soc. Symp. Proc., 1992), Vol. 242, p. 623.

[28]T. Sugino, K. Tanioka, S. Kawasaki, and J. Shirafuji, Jpn. J. Appl. Phys., Part 2 **36**, L463 (1997).

[29]A. Many, J. Phys. Chem. Solids **26**, 575 (1965).

[30]J. Clinton, "Optimization and characterization of a novel shelf powered solid state neutron detector," Ph.D. thesis (Rensselaer Polytechnic Institute, New York, USA, 2011), Chap. 3, pp. 73–78.

[31]S. L. Bellinger, R. G. Fronk, T. J. Sobering, and D. S. McGregor, Appl. Radiat. Isot. **70**, 1121 (2012).

[32]H. X. Jiang and J. Y. Lin, ECS J. Solid State Sci. Technol. **6**, Q3012 (2017).